

Cite this: *Nanoscale*, 2011, **3**, 3731

www.rsc.org/nanoscale

PAPER

## High performance, freestanding and superthin carbon nanotube/epoxy nanocomposite films†

Jinzhu Li,<sup>a</sup> Yun Gao,<sup>b</sup> Wenjun Ma,<sup>c</sup> Luqi Liu,<sup>b</sup> Zhong Zhang,<sup>b</sup> Zhiqiang Niu,<sup>a</sup> Yan Ren,<sup>a</sup> Xiaoxian Zhang,<sup>d</sup> Qingshen Zeng,<sup>d</sup> Haibo Dong,<sup>a</sup> Duan Zhao,<sup>a</sup> Le Cai,<sup>a</sup> Weiya Zhou<sup>a</sup> and Sishen Xie<sup>\*a</sup>

Received 29th April 2011, Accepted 10th June 2011

DOI: 10.1039/c1nr10438a

We develop a facile, effective and filter free infiltration method to fabricate high performance, freestanding and superthin epoxy nanocomposite films with directly synthesized Sing-Walled Carbon Nanotubes (SWNTs) film as reinforcement skeleton. It is found that the thicknesses of the nanocomposite films can be easily controlled in the range of 0.5–3  $\mu\text{m}$  by dripping target amount of acetone diluted epoxy through the skeleton film. The consequent measurements reveal that the mechanical and electrical properties of SWNTs/epoxy nanocomposite films could be tailored in a quite wide range. For examples, the Young's modulus of nanocomposite films can be tuned from 10 to 30 GPa, and the electrical conductivity can be ranged from 1000  $\text{S}\cdot\text{cm}^{-1}$  to be insulated. Moreover, high load transfer efficiency in the nanocomposite films is demonstrated by the measured ultrahigh Raman bands shift rate ( $-30 \pm 5 \text{ cm}^{-1}/\%$  strain) under strain. The high effective modulus is derived as  $774 \pm 70$  GPa for SWNTs inside this nanocomposite film.

### Introduction

Thanks to their exceptional mechanical and electrical performances, SWNTs have been the focus of theory and experiment research for the last two decades and supposed as one of the most promising candidates for lightweight multifunctional composites with enhanced properties.<sup>1–7</sup>

Various nanotube–polymer composite films or bulks prepared by different techniques can be simply divided into two types according to the existing form of the carbon nanotubes (CNTs) in the final composites. One type is the traditional composite bulks using dispersed CNTs as reinforcing filler fabricated by solution mixing or melt blending processing, which usually has problems such as inadequate volume fraction, bad dispersion and lack of effective interface between the components of the composite.<sup>6–10</sup> The other type is the composites using pre-forming entangled CNTs networks as reinforcement scaffolds during the composite process like Buckypaper based soaking or vacuum-aided solution

infiltration,<sup>11–13</sup> in which high CNTs loading and more effective load transfer can be easily obtained. However, all these composites based on dispersed CNTs or following Buckypaper need a good dispersion of CNTs in solution with the aid of surfactant, sonication and further processes like full vacuum infiltration and so forth. Furthermore, inter-bundle slide occurs easily since the interface between CNTs bundles self-assembly by van der Waals force during Buckypaper filtration in the networks is so poor.<sup>12</sup> Therefore, both a facile and biocompatible fabrication method and a load transfer favoured system are urgently needed. Recently, multifunctional composite films or bulks based on directly synthesized CNTs films and forests (or aligned arrays) have attracted increasing attention for their facile fabrication and highly enhanced multifunctional properties.<sup>14–18</sup>

As a non-destructive and environmentally powerful tool, resonance Raman spectra (RRS) has been widely used to characterize the CNTs based composites. Following the Raman band frequency and intensity variations under strain, one can gain the level of load transfer efficiency and effective modulus of the CNTs reinforcement in the composite.<sup>19–25</sup>

In our previous work, we reported a strong, highly conducting and transparent large-area freestanding SWNTs films grown by floating catalyst chemical vapor deposition (FCCVD).<sup>26,27</sup> The electrical conductivity of this SWNTs film is over 2000  $\text{S}\cdot\text{cm}^{-1}$  while the modulus and tensile strength of it are up to 5 GPa and 360 MPa, respectively. These superior electrical and mechanical properties provide them wide opportunities for applications such as super strong pure and composite fibers and the electrode materials for electrochemical supercapacitors.<sup>28–30</sup>

<sup>a</sup>Beijing National Laboratory for Condensed Matter Physics, Institute of Physics, Chinese Academy of Sciences, Beijing, 100190, P. R. China. E-mail: sxxie@aphy.iphy.ac.cn; Fax: +86-10-82640215; Tel: +86-10-82649081

<sup>b</sup>National Center for Nanoscience and Technology, Beijing, P. R. China

<sup>c</sup>Max Planck Institute of Quantum Optics, D-85748 Garching, Germany

<sup>d</sup>Key Laboratory for the Physics and Chemistry of Nanodevices and Department of Electronics, Peking University, Beijing, P. R. China

† Electronic supplementary information (ESI) available: Optical and SEM images of pure as grown SWNTs film; The resistance change versus the tensile strain (stress) curve for the composite film. See DOI: 10.1039/c1nr10438a

Here, we use it to fabricate a high performance, freestanding, superthin and high SWNTs loading epoxy nanocomposite film using a new substrate and filter free infiltration method. These porous and freestanding as grown SWNTs films were introduced as a reinforcement skeleton, and acetone diluted epoxy resin was infiltrated through the SWNT films along their thickness direction (As seen in Fig. 1a). Morphology characterization demonstrated that the epoxy molecular has penetrated through the whole SWNTs film and formed a continuous interpenetrating reticulate architecture like a nanoscale ferroconcrete. Mechanical, electrical and further Raman characterizations under strain have been carried out on the nanocomposite films. Our results reveal that their thickness dependent mechanical and electrical properties can be easily tailored in a quite wide range. Moreover, high load transfer efficiency can be implied by the measured ultrahigh Raman band shift rate and the corresponding derived high effective modulus of the SWNTs in the composite film.

## Experimental details

### Fabrication of the SWNTs film/epoxy composite film

For protecting the natural inter-bundle bond structure in the pure SWNTs film, no purification or surface chemical modification procedure was applied owing to its double-edged effect. On one side, it will indeed introduce some functional groups and form a better chemical adhesion to the polymer matrix, which is helpful to improve the load transfer efficiency and the mechanical properties of the final composites.<sup>7,10</sup> On the other side, it could also significantly degrade the wall structure of SWNTs and result in weakening or shortening of the CNTs, which may depress the mechanical properties of final composites.<sup>19</sup>

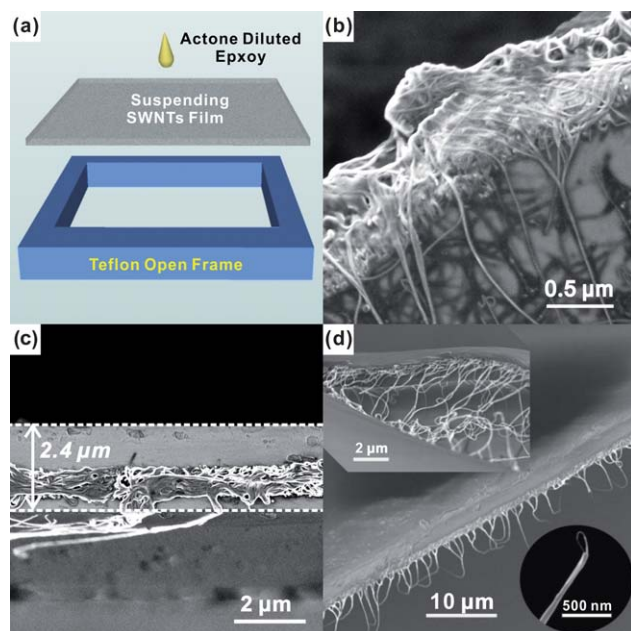


**Fig. 1** Fabrication and morphology of the composite films. (a) Schematic illustration of the fabrication procedure for the SWNTs film/epoxy composite film. (b) & (c) SEM images of the cross sections for two final composite films with thickness about 0.5  $\mu\text{m}$  and 2.4  $\mu\text{m}$ , respectively. (d) SEM images of fracture surface after the mechanical or Raman testing.

To fabricate the SWNTs/epoxy composite film, a facial CNTs networks based infiltration method was adopted. As seen in Fig. 1a, firstly a piece of as grown pure SWNTs film was tightly mounted on an open frame (30  $\times$  30 mm) (Optical images see Supplementary Information Fig. S1). Then one drop (10  $\mu\text{l}$ ) of the acetone solution contained 5–10 w/w% of epoxy constituents (monomer and curing agent mixture) was dripped on the film surface with a high resolution pipette (Eppendorf Research 0.5–10  $\mu\text{l}$ ). Owing to the good affinity, porous structure and the nanoscale thickness of the pure SWNTs film, the dripped solution would immediately spread and wet the whole film skeleton (see Supplementary Information Fig. S2). After the target volume of solution had been infiltrated through the film by multiple treatments, the frame with film was left to dry in a vacuum oven at 60  $^{\circ}\text{C}$  for one hour to evaporate the extra acetone and then be cured with the same procedures to fabricate the composite fibers in our earlier work.<sup>28</sup> This facile and effective fabrication method advances in many aspects. Firstly, comparing with other dispersed CNTs and Buckypaper based processes, this method is more facile and biocompatible because our new process is free from the chemical sufferings such as chemical dispersion of the SWNTs, the aid of surfactant, sonication and full vacuum infiltration, *etc.* Secondly, the thicknesses of the composite films can be easily controlled in the range of 0.5–3  $\mu\text{m}$  depending on the thicknesses of pure SWNTs films as well as the concentration and amount of the solution filtrated through the films, which is difficult for soaking-infiltrating method. As a result, thickness dependent properties such as loading fraction of the SWNTs, mechanical, electrical performance and optical transparency can be effectively tailored. Furthermore, since mechanical or chemical elimination of the substrates or filters often combines with the introduction of inevitable surface micro flaws, this facile, effective, substrate and filter free procedure permits the fabrication of freestanding, superthin, high CNTs loading composite film with tuneable mechanical and electrical properties.

### Characterization

Before performing mechanical and Raman tests, the composite films were cut into strips with the same dimensions. Morphology of the composite films including the cross sections and fracture surfaces were carried out by a Hitachi S5200 Scanning Electron Microscopy (SEM) system. Mechanical tests were performed in a TA Instruments Dynamic Mechanical Analyzer Q800 (the maximum force can sustain is 18 N). For consistency, all mechanical tests were implemented on specimens with the same gauge dimensions of 10  $\times$  3 mm and at the same strain rate of 1%  $\text{min}^{-1}$ . DC electrical conductivities were measured using Keithley 4200-SCS under ambient condition. Raman spectra under continuous strain were obtained using a Renishaw *in via* Raman spectra system equipped with a 632.8 nm helium-neon laser and pre-calibrated with the 520  $\text{cm}^{-1}$  peak of silicon. The resolution of the spectrometer is about 1  $\text{cm}^{-1}$ . Accurately continuous change of strain loaded along the long axis of the specimen was realized by a homemade one-dimension tensile flat equipped with a micrometer.

## Results and discussion

### Morphology

With this facile procedure, the total thicknesses of the final composite films can be easily controlled in the range of 0.5–3  $\mu\text{m}$ . Considering the as-grown pure SWNTs films chosen here have an average thickness of 300 nm and free volume of 30%, the approximately estimated volume fractions of SWNTs are in a wide range from 7% to 40%. Combining the densities of 1.33  $\text{g cm}^{-3}$  and 1.9  $\text{g cm}^{-3}$  for the SWNTs and polymer, respectively, the corresponding mass fractions of SWNTs inside the composite films range about from 5% to 32%. Fig. 1b & c give the typical cross sections SEM images of two composite films with thickness about 0.5  $\mu\text{m}$  and 2.4  $\mu\text{m}$ , indicating corresponding volume (mass) fractions of SWNTs are about 8% (6%) and 40% (32%), respectively. The fracture surface SEM images of the composite film after the mechanical or Raman testing are shown in Fig. 1d. The top left inset shows a microcrack connected by polymer coated CNTs structure. Although most of CNTs bundles broke together with epoxy enveloped on their surfaces making a brittle fracture behaviour, pull-out phenomenon of the CNTs was also found, implying some plastic deformation of this composite film before its final fracture under large strain (see Fig. 2a). However, it should be noticed that this pull-out is not hair-like pure CNTs or their bundles but always with epoxy sheathed on the surface, which can be seen in the enlarged SEM image of the fracture tip (shown in the lower right inset of Fig. 1d). Based on the above results, we conclude that the epoxy

molecular has penetrated through the whole SWNTs film skeleton and formed a continuous interpenetrating reticulate architecture like a nanoscale ferroconcrete. On one hand, the continuous reticulate architecture of the skeleton film was maintained in the fabrication process, which also provides reinforcement skeletons and paths in the final composite film. On the other hand, the epoxy molecules have effectively intercalated the nanoscale vacancies of the SWNTs film skeleton (see Supplementary Information Fig. S2)<sup>†</sup> and entangled with the CNTs bundles or the inter-bundle shear-legs, making this nanocomposite film like a stronger nanoscale ferroconcrete.

### Mechanical tests

Due to the especial structure of the composite film, one point should be noticed. Since the mechanical properties of pure epoxy are much lower than the composite film even the pure SWNTs film, most of the stress loaded on the specimen is carried by the middle true effective composite zone. Therefore, the mechanical property of this composite film is expected to be tuneable by adjusting its total thickness. When there are extra pure epoxy layers on both sides of the middle true effective composite zone, we can treat the combination as a multilayer stack made from uniform films. Its equivalent two-dimensional elastic stiffness is:<sup>14</sup>

$$\bar{E}t = \sum_{i=1}^n E_i t_i = E_0 t_0 + E_1 (t - t_0) \quad (1)$$

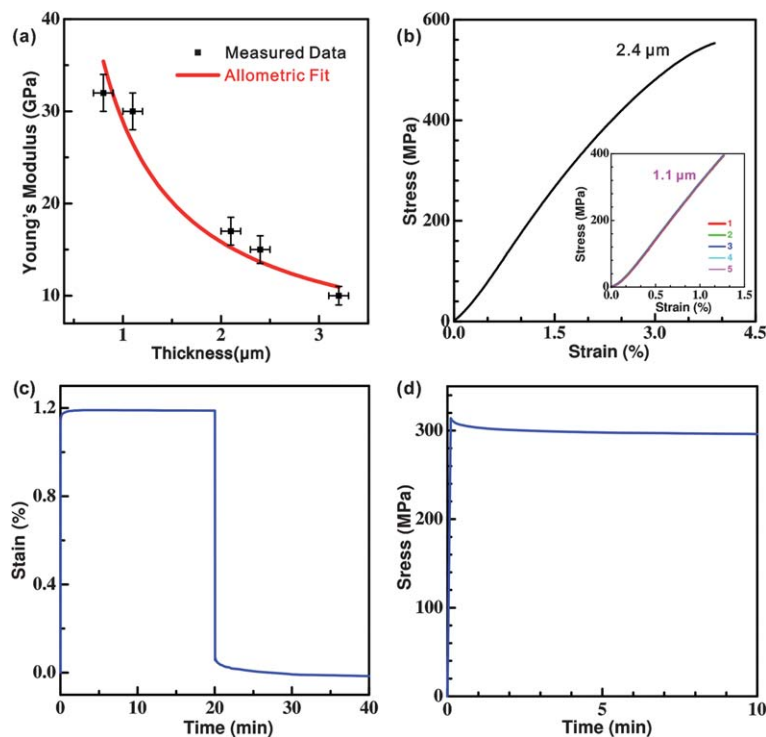


**Fig. 2** Mechanical tests of the composite films. (a) Young's modulus *versus* total thickness of the composite film. Solid red line is the best fitting line with eqn (2). (b) Typical stress-strain curve for a composite film with a thickness about 2.4  $\mu\text{m}$ . Inset gives the stress-strain curves of multi-times tensile tests below 1.5% for a 1.1  $\mu\text{m}$  thick composite film. (c) Typical creep and recovery curve of the composite film at initial strain 1.16% (constant stress 300 MPa). (d) Relaxation curve for the composite film (constant strain 1.2%).

Where  $E_0$  and  $t_0$  are the elastic modulus and thickness of the middle true effective composite zone,  $E_1$  is modulus of pure epoxy (2.8 GPa), So the relationship between average modulus  $\bar{E}$  and total thickness  $t$  of the whole composite film can be expressed by an allometric function as follows:

$$\bar{E} = t^{-1}[E_0 t_0 + E_1(t - t_0)] = E_1 + \alpha t^{-1} \quad (2)$$

Fig. 2a is the Young's modulus *versus* total thickness of the composite film. Fits to the measured data using eqn (2) provide good agreement with the experimental data. From this we can conclude that by adjusting the thickness of the composite films in the range of 0.5–3  $\mu\text{m}$ , the Young's modulus of the composite film can be easily tuned in a quite wide range from 10 to 30 GPa, which is about one order of magnitude higher than the pure epoxy bulk. As far as we know, these values are one of the highest in the CNTs-based composite bulks or films and similar with the high CNTs volume fraction composite bulks from layer-by-layer (LBL) method.<sup>4</sup> What is more, in our facile fabrication process, there was neither need of dispersion or functionalization procedures nor further substrate delamination assisted by environmental unfriendly acid or other materials. A typical stress-strain curve for a composite film with a thickness about 2.4  $\mu\text{m}$  is shown in Fig. 2b. We can see that the measured Young's modulus and tensile strength are about 15 GPa and 550 MPa while the final strain is 3.8%. Besides, its corresponding tensile toughness (total integrated area under the stress-strain curve) is about 11 MPa, which is about 18 times of that for pure epoxy bulk (0.6 MPa) and little lower than that of pure SWNTs film (15 MPa<sup>27</sup>). Since the tensile toughness is the energy of the system absorbed in the deformation process, thus we can draw the conclusion that the SWNTs film skeleton dominates the deformation energy absorption as well as the load transfer. Inset in Fig. 2b gives the stress-strain curves of multi-times tensile tests below 1.5% for a composite film with a thickness of 1.1  $\mu\text{m}$  and modulus about 30 GPa, indicating the high elasticity and repeatability in this low strain region. Besides, from the typical creep and recovery curve (see Fig. 2c), we can find that there is a very little elongation (less than 0.03%) within twenty minutes and no residue strain after the withdrawing of the constant stress. Meanwhile, from the relaxation curve shown in Fig. 2d, we can see the stress decrease is also very little and slow, which further demonstrates that the tensile deformation of composite film in this low strain region can be supposed as pure elastic. These outstanding tuneable mechanical performances of the nanocomposite film such as high modulus, strength and elasticity give it great potential applications for long-lifetime components in the aircraft and automobile industries.

### Electrical characterization

Since the electrical conductivity of the pure SWNTs film is as high as 2000  $\text{S cm}^{-1}$  while the pure epoxy used here is absolute insulated, the electrical performance of the composite film should also be thickness dependent just like the mechanical properties. Fig. 3a gives the  $I$ - $V$  curve for a square composite film with thickness about 1  $\mu\text{m}$ , and corresponding electrical conductivity is still up to 170  $\text{S cm}^{-1}$ . This value is one order of magnitude lower than that of the pure SWNTs film, but several orders of

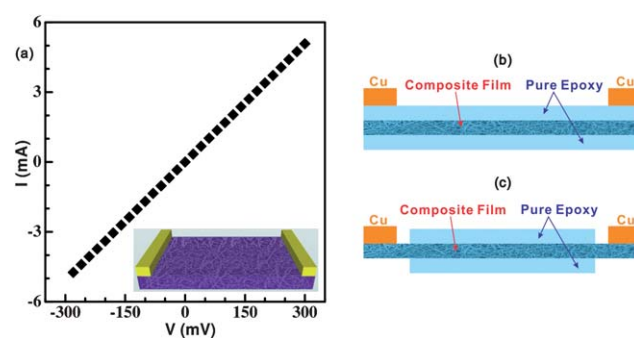


**Fig. 3** Electrical characterization of the composite films. (a)  $I$ - $V$  curve for a square composite film with a thickness about 1  $\mu\text{m}$ , inset is the sketch of the measurement. (b)&(c) Sketch drawings for the electrical characterization with different electrodes embedded ways.

magnitude higher than that for the traditional dispersed CNTs based composite films or bulks.<sup>31,32</sup> Whereas, for a 2.4  $\mu\text{m}$  thick composite film (shown in Fig. 1c), extra pure epoxy layers coated on both sides dramatically depress the surface conductivity even to be insulated (measurement sketch see Fig. 3b). That is, the surface electrical performance of the composite film can also be easily tailored in a wide range from being highly conductive to totally insulated. We believe that the high conductivity of the thinner composite film originates from the high SWNTs loading in the composite and the unbroken continuous paths supplied by the SWNTs film skeleton. In addition, results taken from dozens of samples with pre-embedded Cu electrodes (see Fig. 3c) show that the resistances are only about twice their values before the infiltration of epoxy, which means the corresponding conductivity is about 1000  $\text{S cm}^{-1}$ . This little decrease of electrical conductivity further implies that the good entanglement interaction has indeed formed between epoxy molecular and the CNTs bundles or junctions, but the mechanical or electrical paths supplied by the SWNTs film skeleton are still maintained. Moreover, we studied the resistance dependence on the tensile strain (or stress). Our results elucidate that the resistance of the composite film increases with the tensile strain (or stress) and exhibits perfect reversibility and repeatability in the low elastic range of 2.8% (Supplementary Fig. S3)†, providing this composite film high potential for many applications such as elastic and stretchable electrics<sup>33</sup> and strain (stress) sensor,<sup>34</sup> *etc.*

### In situ Raman spectra under continuous strain

To follow the load transfer efficiency in this composite film, we measured the  $G'$  Raman band downshift as a function of applied strain since it is the most sensitive Raman band for the extra strain.<sup>35,36</sup> It was reported that the Raman bands downshift nearly linearly with the applied uniaxial strain, but only in a very low elastic strain range below 1% for dispersed CNTs reinforced composites. Beyond this, the Raman bands are almost no longer changed because of interface slippage between the dispersed CNTs and the polymer matrix.<sup>19–23</sup> Here, special continuous interpenetrating reticulated architecture in our composite film should be favourable for decreasing the slippage and improving the load transfer efficiency. Even so, our Raman and mechanical

test results show that this elastic region is no higher than 3%. So in this paper we focus on the high-elastic region below 1%.

Fig. 4a gives the  $G'$  Raman band spectra stack of one specimen under continuous strain. With increasing strain from 0% to 1%, the  $G'$  band downshifts by  $33\text{ cm}^{-1}$ . This significant downshift can be easily explained by that the effective elongation of the C–C bond length induced by extra force could weaken the bond thus lower its vibrational frequency.<sup>35,36</sup> Subsequently, the strain decreases from 1% to 0% and the  $G'$  Raman band upshifts to its original frequency. Fig. 4b is the  $G'$  Raman band downshift as a function of strain applied on the specimen, from which we can obtain that with the variation of strain, the  $G'$  Raman band downshifts linearly with a best fitting slope as high as  $-33\text{ cm}^{-1}/\%$  strain and upshifts with almost the same value.

Interestingly, when the strain are completely unloaded, the  $G'$  band frequency returns to its original position with unobvious variation, even the strain is back to zero abruptly from a high strain. Furthermore, repeated measurements verified the reversibility of the Raman band shift, displaying that the deformation in this region is totally elastic, which is also confirmed by the mechanical results (Fig. 2). Moreover, the D/G band intensity ratio has nearly no vibration in these deformation processes, also implies that the SWNTs only have revisable and repeatable geometry changes without any introduction of structural defects. This high precise relationship between Raman band frequency and the strain makes this composite film a promising candidate for strain or stress sensor.

### High effective modulus derived from Raman results

After massive analysis on hundreds of Raman spectra for dozens of specimens, we obtain that the  $G'$  Raman band shift rates are in the range of  $-30 \pm 5\text{ cm}^{-1}/\%$  strain, which almost approach the level of that for individual SWNTs<sup>35,36</sup> and suppress the results from dispersed-SWNTs reinforced composite films or bulks.<sup>20–23</sup>

It is evidenced this average Raman band downshift rate for CNTs assembles and their composites is dependent on many

factors including the laser polarization configuration, angular quantity distribution of CNTs as well as the angles between the nanotube axes, strain and laser polarization directions.<sup>22–24</sup> In particular, when the strain direction is parallel to the polarization direction of incident laser under  $VV$  configuration (polarization directions of incident laser and scattered light are parallel), the measured average Raman band shift rate  $S_{VV}(0,0)$  and the ideal Raman band shift rate  $S_0$  (when all the nanotubes are parallel to the strain direction) have a relationship of  $S_{VV}(0,0) = \eta S_0$ . For a uniformly distributed 2D system, coefficient  $\eta$  is 0.77.<sup>24</sup> However, the CNTs bundles in our pure film skeletons are not randomly distributed but have certain orientation along the gas flow when they were growing in the reaction zone (see Supplementary Information Fig. S2). Thus a revised value of  $\eta$  (0.7–0.82) was adopted for different angles between the preferred orientation direction and the strain direction. Additionally, it was reported that the Raman  $G'$  band downshift rate is proportional to the effective modulus of the carbon reinforcement in the composites, with a proportional coefficient of  $-0.05\text{ cm}^{-1}/\text{GPa}\%$ .<sup>22</sup> Based on the measured  $S_{VV}(0,0) = -30 \pm 5\text{ cm}^{-1}/\%$  strain, we can obtain the ideal Raman band shift rate  $S_0 = -39.2 \pm 3.5\text{ cm}^{-1}/\%$  strain and the effective modulus of the SWNTs  $E_{\text{eff}} = 774 \pm 70\text{ GPa}$ , which approaches the theory value 1 TPa and elucidates that the mechanical properties of the SWNTs in the composite films have been effectively expressed.

### Conclusions

In conclusion, developing directly synthesized pure SWNTs film as skeleton, a substrate and filter free infiltration method has been developed to fabricate high performance, freestanding, superthin and high SWNTs loading percentage epoxy composite film. *Via* controlling the total thicknesses (0.5–3  $\mu\text{m}$ ) of the nanocomposite films by dripping target volume of solution through the film skeleton, their Young's modulus can be tuned in the range of 10–30 GPa and the electrical conductivity can be ranged from  $1000\text{ S cm}^{-1}$  to be insulated. This facile and effective method combined with attractive tuneable mechanical and electrical properties give the nanocomposite film lots of potential applications such as coating and lamination materials, electromagnetic shielding materials, film electrodes, electromechanical actuators and so on. In addition, the high Raman band shift rate ( $-30 \pm 5\text{ cm}^{-1}/\%$  strain) and the derived high effective modulus ( $774 \pm 70\text{ GPa}$ ) imply the high load transfer efficiency in this nanocomposite, and indicate the potential of our ultrathin films acting as stress or strain sensors.

### Acknowledgements

This work is supported by the Beijing Municipal Education Commission (Grant No. YB20108000101), the Key Item of Knowledge Innovation Project of Chinese Academy of Sciences (KJCX2-YW-M01), the National Natural Science Foundation of China (Grant No. 90921012) and the National Basic Research Program of China (Grant No. 2005CB623602).

### References

- 1 M. M. J. Treacy, T. W. Ebbesen and J. M. Gibson, *Nature*, 1996, **381**, 678–680.

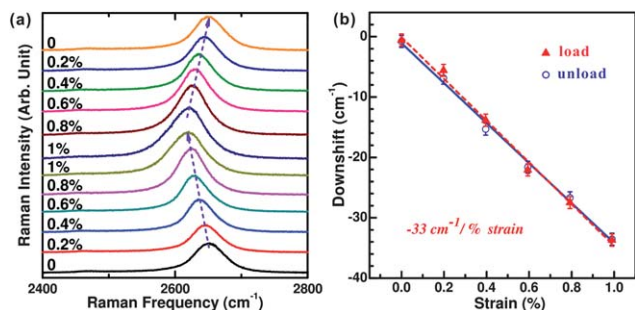


**Fig. 4** *In situ* Raman characterization under continuous strain (a) The  $G'$  Raman band spectra stack with the increase of strain from 0% to about 1% and then decreases to 0% (from bottom to up). The intensity has arbitrary unit. (b) The  $G'$  Raman band downshift as a function of applied strain. The bands frequencies are obtained by Gauss-Lorentz fitting of the spectra in (a). The red solid up-triangles and blue open circles represent the downshift and upshift processes, corresponding to the load and unload of the strain, respectively. The red dashed line and blue solid line are the best fitting slopes for downshift and upshift processes.

- 2 M. F. Yu, B. S. Files, S. Arepalli and R. S. Ruoff, *Phys. Rev. Lett.*, 2000, **84**, 5552–5555.
- 3 V. L. Pushparaj, M. M. Shaijumon, A. Kumar, S. Murugesan, L. Ci, R. Vajtai, R. J. Linhardt, O. Nalamasu and P. M. Ajayan, *Proc. Natl. Acad. Sci. U. S. A.*, 2007, **104**, 13574–13577.
- 4 A. A. Mamedov, N. A. Kotov, M. Prato, D. M. Guldi, J. P. Wicksted and A. Hirsch, *Nat. Mater.*, 2002, **1**, 190–194.
- 5 G. Zou, M. Jain, H. Yang, Y. Zhang, D. Williams and Q. Jia, *Nanoscale*, 2010, **2**, 418–422.
- 6 R. H. Baughman, A. A. Zakhidov and W. A. de Heer, *Science*, 2002, **297**, 787–792.
- 7 J. N. Coleman, U. Khan, W. J. Blau and Y. K. Gun'ko, *Carbon*, 2006, **44**, 1624–1652.
- 8 P. M. Ajayan and J. M. Tour, *Nature*, 2007, **447**, 1066–1068.
- 9 M. S. P. Shaffer and A. H. Windle, *Adv. Mater.*, 1999, **11**, 937–941.
- 10 L. Q. Liu, A. H. Barber, S. Nuriel and H. D. Wagner, *Adv. Funct. Mater.*, 2005, **15**, 975–980.
- 11 J. N. Coleman, W. J. Blau, A. B. Dalton, E. Munoz, S. Collins, B. G. Kim, J. Razal, M. Selvidge, G. Viegro and R. H. Baughman, *Appl. Phys. Lett.*, 2003, **82**, 1682–1684.
- 12 Z. Wang, Z. Y. Liang, B. Wang, C. Zhang and L. Kramer, *Composites, Part A*, 2004, **35**, 1225–1232.
- 13 Z. Spitalsky, G. Tsoukleri, D. Tasis, C. Krontiras, S. N. Georga and C. Galiotis, *Nanotechnology*, 2009, **20**, 405702.
- 14 L. Song, H. Zhang, Z. Zhang and S. S. Xie, *Composites, Part A*, 2007, **38**, 388–392.
- 15 M. K. Shin, J. Oh, M. Lima, M. E. Kozlov, S. J. Kim and R. H. Baughman, *Adv. Mater.*, 2010, **22**, 2663–2667.
- 16 L. Ci, J. Suhr, V. Pushparaj, X. Zhang and P. M. Ajayan, *Nano Lett.*, 2008.
- 17 Q. F. Cheng, J. P. Wang, J. J. Wen, C. H. Liu, K. L. Jiang, Q. Q. Li and S. S. Fan, *Carbon*, 2010, **48**, 260–266.
- 18 H. Huang, C. H. Liu, Y. Wu and S. S. Fan, *Adv. Mater.*, 2005, **17**, 1652–1656.
- 19 N. Lachman, C. Bartholome, P. Miaudet, M. Maugey, P. Poulin and H. D. Wagner, *J. Phys. Chem. C*, 2009, **113**, 4751–4754.
- 20 X. F. Zhang, T. Liu, T. V. Sreekumar, S. Kumar, V. C. Moore, R. H. Hauge and R. E. Smalley, *Nano Lett.*, 2003, **3**, 1285–1288.
- 21 L. S. Schadler, S. C. Giannaris and P. M. Ajayan, *Appl. Phys. Lett.*, 1998, **73**, 3842–3844.
- 22 C. A. Cooper, R. J. Young and M. Halsall, *Composites, Part A*, 2001, **32**, 401–411.
- 23 M. D. Frogley, Q. Zhao and H. D. Wagner, *Phys. Rev. B: Condens. Matter*, 2002, **65**, 113413.
- 24 L. B. Deng, S. J. Eichhorn, C. C. Kao and R. J. Young, *ACS Appl. Mater. Interfaces*, 2011, **3**, 433–440.
- 25 Y. Gao, J. Z. Li, L. Q. Liu, W. J. Ma, W. Y. Zhou, S. S. Xie and Z. Zhang, *Adv. Funct. Mater.*, 2010, **20**, 3797–3803.
- 26 L. Song, L. Ci, L. Lv, Z. P. Zhou, X. Q. Yan, D. F. Liu, H. J. Yuan, Y. Gao, J. X. Wang, L. F. Liu, X. W. Zhao, Z. X. Zhang, X. Y. Dou, W. Y. Zhou, G. Wang, C. Y. Wang and S. S. Xie, *Adv. Mater.*, 2004, **16**, 1529–1532.
- 27 W. J. Ma, L. Song, R. Yang, T. H. Zhang, Y. C. Zhao, L. F. Sun, Y. Ren, D. F. Liu, L. F. Liu, J. Shen, Z. X. Zhang, Y. J. Xiang, W. Y. Zhou and S. S. Xie, *Nano Lett.*, 2007, **7**, 2307–2311.
- 28 W. J. Ma, L. Q. Liu, Z. Zhang, R. Yang, G. Liu, T. H. Zhang, X. F. An, X. S. Yi, Y. Ren, Z. Q. Niu, J. Z. Li, H. B. Dong, W. Y. Zhou, P. M. Ajayan and S. S. Xie, *Nano Lett.*, 2009, **9**, 2855–2861.
- 29 W. J. Ma, L. Q. Liu, R. Yang, T. H. Zhang, Z. Zhang, L. Song, Y. Ren, J. Shen, Z. Q. Niu, W. Y. Zhou and S. S. Xie, *Adv. Mater.*, 2009, **21**, 603–608.
- 30 Z. Q. Niu, W. Y. Zhou, J. Chen, G. X. Feng, H. Li, W. J. Ma, J. Z. Li, H. B. Dong, Y. Ren, D. A. Zhao and S. S. Xie, *Energy Environ. Sci.*, 2011, **4**, 1440–1446.
- 31 J. Sandler, M. S. P. Shaffer, T. Prasse, W. Bauhofer, K. Schulte and A. H. Windle, *Polymer*, 1999, **40**, 5967–5971.
- 32 B. E. Kilbride, J. N. Coleman, J. Fraysse, P. Fournet, M. Cadek, A. Drury, S. Hutzler, S. Roth and W. J. Blau, *J. Appl. Phys.*, 2002, **92**, 4024–4030.
- 33 J. A. Rogers, T. Someya and Y. G. Huang, *Science*, 2010, **327**, 1603–1607.
- 34 T. Yamada, Y. Hayamizu, Y. Yamamoto, Y. Yomogida, A. Izadi-Najafabadi, D. N. Futaba and K. Hata, *Nat. Nanotechnol.*, 2011, **6**, 296–301.
- 35 S. B. Cronin, A. K. Swan, M. S. Unlu, B. B. Goldberg, M. S. Dresselhaus and M. Tinkham, *Phys. Rev. B: Condens. Matter Mater. Phys.*, 2005, **72**, 035425.
- 36 S. B. Cronin, A. K. Swan, M. S. Unlu, B. B. Goldberg, M. S. Dresselhaus and M. Tinkham, *Phys. Rev. Lett.*, 2004, **93**, 167401.